Investigations of moiré artifacts induced by flux fluctuations in x-ray dark-field imaging

Zhi-Li Wang(王志立)[1,†], Zi-Han Chen(陈子涵)[1], Yao Gu(顾瑶)[1], Heng Chen(陈恒)[1], and Xin Ge(葛昕)[2]

[1] *Department of Optical Engineering, School of Physics, Hefei University of Technology, Hefei* 230009, *China*
[2] *Institute of Biomedical Engineering, Shenzhen Bay Laboratory, Shenzhen* 518067, *China*

(Received 23 June 2022; revised manuscript received 3 September 2022; accepted manuscript online 23 September 2022)

X-ray dark-field imaging using a grating interferometer has shown potential benefits for a variety of applications in recent years. X-ray dark-field image is commonly retrieved by using discrete Fourier transform from the acquired phase-stepping data. The retrieval process assumes a constant phase step size and a constant flux for each stepped grating position. However, stepping errors and flux fluctuations inevitably occur due to external vibrations and/or thermal drift during data acquisition. Previous studies have shown that those influences introduce errors in the acquired phase-stepping data, which cause obvious moiré artifacts in the retrieved refraction image. This work investigates moiré artifacts in x-ray dark-field imaging as a result of flux fluctuations. For the retrieved mean intensity, amplitude, visibility and dark-field images, the dependence of moiré artifacts on flux fluctuation factors is theoretically derived respectively by using a first-order Taylor series expansion. Results of synchrotron radiation experiments verify the validity of the derived analytical formulas. The spatial frequency characteristics of moiré artifacts are analyzed and compared to those induced by phase-stepping errors. It illustrates that moiré artifacts can be estimated by a weighted mean of flux fluctuation factors, with the weighting factors dependent on the moiré phase and different greatly for each retrieved image. Furthermore, moiré artifacts can even be affected by object's features not displayed in the particular contrast. These results can be used to interpret images correctly, identify sources of moiré artifacts, and develop dedicated algorithms to remove moiré artifacts in the retrieved multi-contrast images.

Keywords: x-ray imaging, dark-field imaging, moiré artifacts, flux fluctuations

PACS: 87.59.–e, 87.64.mf, 87.57.cp, 87.57.N– **DOI:** 10.1088/1674-1056/ac946a

1. Introduction

In the field of x-ray phase imaging, x-ray grating interferometry has attracted increasing attention from the scientific community,[1–18] since it can be implemented with conventional tube sources and detectors.[2,3] As a multi-contrast technique, x-ray grating interferometry simultaneously provides the transmission, refraction (i.e., differential phase) and dark-field images of the investigated object.[3] The additional refraction and dark-field images offer the potential of complementary information. The refraction signal features improved soft-tissue contrast, while the dark-field signal enables the detection of unresolved microstructures below the spatial resolution of x-ray grating interferometer.[6] Over the past decades, x-ray grating interferometry has shown significant potential in diverse applications including, but not limited to: mammography,[19,20] cardiovascular imaging,[21] materials science,[22,23] non-destructive testing,[24,25] detection of foreign bodies,[26] and chest imaging for early detection of pulmonary emphysema.[27–29]

In x-ray grating interferometry, the phase-stepping technique is commonly used for data acquisition.[1–3] The phase-stepping technique is achieved by stepwise translating one of the gratings and acquiring an intensity image at each scanned grating position. Transmission, refraction and dark-field images of the object can be retrieved from the acquired phase-stepping data using discrete Fourier transform[1–3] or a least-squares fitting algorithm.[30] The retrieval process assumes that a constant x-ray flux is utilized for each phase step, and a constant step size equals to a fraction of the grating period. However, flux fluctuations and phase stepping errors unavoidably occur during the phase-stepping process. They can be induced by the instability of the x-ray source, the thermal drift, vibrations and mechanical inaccuracies of x-ray grating interferometer. Flux fluctuations and phase-stepping errors cause intensity variations in the acquired phase-stepping data. These variations introduce moiré artifacts in the retrieved images. The resulting moiré artifacts make the image interpretation ambiguous in practical applications, and impede further image post-processing algorithms. Therefore, it becomes quite necessary to quantify the amplitude and the shape of moiré artifacts induced by flux fluctuations and/or phase-stepping errors. This knowledge can be useful for image artifact removal and image interpretation.

To deal with the effect of phase-stepping errors, Hauke *et al.* utilized a Taylor series expansion to derive moiré artifacts of the intensity, phase, amplitude and visibility images in a single phase-stepping.[31] Their results revealed that while the strength of moiré artifacts was different from each retrieved

[†]Corresponding author. E-mail: dywangzl@hfut.edu.cn

© 2023 Chinese Physical Society and IOP Publishing Ltd

image, the basic shape of moiré artifacts was determined by the moiré phase. Alternatively, Marco *et al.* presented a theoretical explanation for the correlation between the phase of the phase stepping curve and moiré artifacts induced by the phase-stepping jitter in all three retrieved modalities.[32] Based on these correlations, they developed a correction algorithm that was able to eliminate the moiré artifacts without degrading true image information. Recently, Hashimoto *et al.* analyzed the moiré artifact of the retrieved refraction image as a result of flux fluctuations and the phase-stepping errors with a different technique.[33] They also proposed an improved algorithm to estimate the flux fluctuations and stepping errors, and remove the moiré artifact in the retrieved refraction image. Quite recently, Viermetz *et al.* presented x-ray dark-field CT results of a human-sized anthropomorphic body phantom by integrating a Talbot–Lau interferometer into a clinical CT gantry.[34] To suppress the artifacts induced by drifts, vibrations and flux fluctuations of the x-ray tube, they developed an iterative optimization which requires prior knowledge including the expected amplitude and frequency of the intensity, phase and visibility variations. However, to the best of our knowledge, there lacks a comprehensive analysis of the effect of flux fluctuations on the variations of retrieved amplitude, visibility and dark-field images. And that will be the subject of this work.

The paper is structured as follows. Section 2 briefly reviews the principle of x-ray dark-field imaging, and then presents theoretical investigations of the influence of flux fluctuations on the retrieved mean intensity, amplitude, visibility and dark-field images, respectively. By using a first-order Taylor series expansion, analytical formulas of moiré artifacts are derived for those distinct retrieved images. In Section 3, we present the results of synchrotron radiation experiments to verify theoretical formulas derived in Section 2. The spatial frequency characteristics of moiré artifacts are discussed and compared to moiré artifacts induced by phase-stepping errors. Finally, we conclude this work in Section 4. We expect that those results can be useful to identify the source of moiré artifacts, and develop dedicated algorithms for artifact correction.

2. Theory and methods

In this section, we first briefly review the theoretical formulas to retrieve x-ray dark-field images and then derive theoretical formulas of moiré artifacts induced by flux fluctuations using the first-order Taylor series expansion.

2.1. Data acquisition and dark-field retrieval

In x-ray grating interferometry, the phase-stepping technique is commonly utilized for data acquisition. One of the gratings is translated stepwise by a fraction of the grating period whereby an intensity image is acquired by the detector at each grating position. Under an ideal situation without flux fluctuations, the measured intensity data can be well approximated by a sinusoidal function for each pixel[31]

$$I_k(x,y) = \bar{I}(x,y) + A(x,y)\cos\left[\frac{2\pi k}{N} + \varphi(x,y) + \varphi_{\mathrm{m}}(x,y)\right], \quad (1 \le k \le N), \tag{1}$$

where (x,y) denotes the pixel coordinates in a two-dimensional detector array, I_k being the measured intensity of the k-th phase step, $\bar{I}$ being the mean intensity, A being the amplitude, N being the total number of phase steps over one grating period, φ being the phase shift induced by the object, and φ_{m} being the moiré phase resulting from the misalignment and local imperfections of the gratings.[31]

In literatures, several algorithms have been developed for retrieval of transmission, refraction and dark-field images from the acquired phase-stepping data.[1–3,16,30] This work investigates the relation of flux fluctuations and the occurrence of moiré artifacts by using the discrete Fourier transform based algorithm.[1–3] For this algorithm, the phase-stepping data is treated as a series of equidistantly sampled sinusoidal functions. As a consequence, one can calculate the mean intensity $\bar{I}$ and the amplitude A respectively by

$$\bar{I}(x,y) = \frac{1}{N}\sum_{k=1}^{N} I_k(x,y), \tag{2}$$

$$A(x,y) = \frac{2}{N}\sqrt{\left[\sum_{k=1}^{N} I_k(x,y)\exp\left(-\mathrm{i}2\pi\frac{k}{N}\right)\right]^2}, \tag{3}$$

from which the visibility V can be retrieved by

$$V(x,y) = A(x,y)/\bar{I}(x,y). \tag{4}$$

Furthermore, the object's transmission signal T and dark-field signal D can be retrieved by calculating these parameters respectively for an object measurement (superscript o) and a reference measurement without object (superscript r)

$$T(x,y) = \bar{I}^{\mathrm{o}}(x,y)/\bar{I}^{\mathrm{r}}(x,y), \tag{5}$$

$$D(x,y) = V^{\mathrm{o}}(x,y)/V^{\mathrm{r}}(x,y). \tag{6}$$

The retrieved transmission and dark-field signals are normally displayed in the form of images.

2.2. Moiré artifact of retrieved dark-field images

Previous work demonstrated that even slight flux fluctuations introduced obvious moiré artifacts into the retrieved refraction image.[33] The following analysis will focus on the moiré artifact induced by flux fluctuations in the retrieved dark-field image. When flux fluctuations are present, a flux fluctuation factor is introduced into Eq. (1), and the measured phase-stepping data can be expressed as follows:

$$I_k(x,y) = \mathrm{e}^{\lambda_k}\left\{\bar{I}(x,y) + A(x,y)\right.$$

$$\times \cos\left[\frac{2\pi k}{N} + \varphi(x,y) + \varphi_{\mathrm{m}}(x,y)\right]\Bigg\}, \quad (1 \le k \le N), \quad (7)$$

where λ_k denotes the flux fluctuation factor of the k-th phase step relative to the first step (i.e., $\lambda_1 = 0$). It should be noted that the relative values between λ_k are of importance since an addition of a constant value to λ_k just introduces a trivial offset into the retrieved mean intensity and amplitude images. This offset can be corrected by normalization.

To estimate the effects of flux fluctuations on the retrieved images, a Taylor series expansion will be used for further analysis. It is assumed that the flux fluctuation factor λ_k is small for all k. Therefore, we can safely apply the first-order Taylor expansion around $\lambda_k = 0$ for all flux fluctuation factors. Note that a similar approximation was made previously for estimations of moiré artifacts induced by phase-stepping errors.[31,32] Before the estimation of moiré artifacts, we tested the validity of our approach. For this purpose, we used our approach to estimate the moiré artifact induced by flux fluctuations in the retrieved refraction image. The obtained result was in agreement with that previously obtained with a different approach.[33] Therefore, the agreement verifies the feasibility of our approach, which can be safely used to proceed with the following calculations.

We estimate the effect of flux fluctuations on the retrieved mean intensity and amplitude images. The image deviations resulting from flux fluctuations are often specified as moiré artifacts.[31–33] Under the above approximations, we can estimate the moiré artifact of the mean intensity image $\Delta\bar{I}$ by

$$\Delta\bar{I} = \sum_{k=1}^{N} \lambda_k \left(\frac{\partial \bar{I}}{\partial \lambda_k}\bigg|_{\lambda_k=0} \right). \quad (8)$$

By using Eqs. (2) and (7), the derivative with respect to the flux fluctuation factor can be expressed as

$$\left(\frac{\partial \bar{I}}{\partial \lambda_k}\bigg|_{\lambda_k=0} \right) = \frac{1}{N} \sum_{k=1}^{N} \left[\bar{I} + A\cos\left(\frac{2\pi k}{N} + \varphi + \varphi_{\mathrm{m}} \right) \right]. \quad (9)$$

By substituting Eq. (9) into Eq. (8), we obtain the analytical expression of the moiré artifact $\Delta\bar{I}$

$$\Delta\bar{I} = \frac{\bar{I}}{N} \left[\sum_{k=1}^{N} \lambda_k + V \sum_{k=1}^{N} \lambda_k \cos\left(\frac{2\pi k}{N} + \varphi + \varphi_{\mathrm{m}} \right) \right], \quad (10)$$

where the indices of the detector pixel coordinates are dropped for clarity. As shown by Eq. (10), the strength of the moiré artifact is proportional to the mean intensity $\bar{I}$. The first term in Eq. (10) contains an unweighted mean of flux fluctuation factors, and is independent of the moiré phase φ_{m}. It introduces a global constant offset in the retrieved mean intensity image. The second term is proportional to the visibility V, and contains a weighted mean of flux fluctuation factors, with the weighting factors dependent on the moiré phase φ_{m}. The second term determines the moiré artifact with a spatial frequency equal to that of the moiré phase φ_{m}. Note that Eq. (10) is quite different from the moiré artifact induced by phase-stepping errors.[31,32] The moiré artifact induced by phase-stepping errors consists of a single term that is proportional to the amplitude A, and has a spatial frequency equal to that of the moiré phase φ_{m}.

Similar to Eq. (8), we can estimate the moiré artifact of the amplitude image ΔA as follows:

$$\Delta A = \sum_{k=1}^{N} \lambda_k \left(\frac{\partial A}{\partial \lambda_k}\bigg|_{\lambda_k=0} \right), \quad (11)$$

where the derivative with respect to the flux fluctuation factor is calculated by using Eqs. (3) and (7),

$$\left(\frac{\partial A}{\partial \lambda_k}\bigg|_{\lambda_k=0} \right) = \frac{2}{N} \cos\left(\frac{2\pi k}{N} + \varphi + \varphi_{\mathrm{m}} \right) \times \left[\bar{I} + A\cos\left(\frac{2\pi k}{N} + \varphi + \varphi_{\mathrm{m}} \right) \right]. \quad (12)$$

Substituting Eq. (12) into Eq. (11) results in the following expression of the moiré artifact ΔA:

$$\Delta A = \frac{1}{N} \left\{ A \sum_{k=1}^{N} \lambda_k + 2\bar{I} \sum_{k=1}^{N} \lambda_k \cos\left(\frac{2\pi k}{N} + \varphi + \varphi_{\mathrm{m}} \right) + A \sum_{k=1}^{N} \lambda_k \cos\left[2\left(\frac{2\pi k}{N} + \varphi + \varphi_{\mathrm{m}} \right) \right] \right\}, \quad (13)$$

where the first term is proportional to the amplitude A and is an unweighted mean of flux fluctuation factors. It determines a global constant offset in the retrieved amplitude image. The second and third terms in Eq. (13) both contain a weighted mean of flux fluctuation factors, with the weighting factors dependent on the moiré phase φ_{m}. The second term is proportional to twice the mean intensity, and introduces moiré artifacts with a spatial frequency equal to that of the moiré phase φ_{m}. By contrast, the third term is proportional to the amplitude A, and results in moiré artifacts with a spatial frequency twice that of the moiré phase φ_{m}. Moreover, it notes that in terms of the spatial frequency, the moiré artifact ΔA in Eq. (13) is quite different from that induced by phase-stepping errors.[31,32] The moiré artifact resulting from phase-stepping errors has a spatial frequency twice that of the moiré phase φ_{m}, and an amplitude proportional to the amplitude A.

Generally, the moiré artifacts $\Delta\bar{I}$ and ΔA are small when compared to $\bar{I}$ and A, respectively. Therefore, we can estimate the moiré artifact of the visibility image ΔV by applying another first-order Taylor expansion with respect to $\bar{I}$ and A. Using Eq. (4), and in equivalence to Eq. (8), the moiré artifact of the visibility image ΔV can be estimated as follows:

$$\Delta V = \frac{\Delta A}{\bar{I}} - \frac{A}{\bar{I}^2}\Delta\bar{I}, \quad (14)$$

which is a superposition of the moiré artifact of the amplitude image and the negative moiré artifact of the mean intensity image. By substituting Eqs. (10) and (13) into Eq. (14), the moiré artifact ΔV can be derived into

$$\Delta V = \frac{1}{N}\left[\left(2-V^2\right)\sum_{k=1}^{N}\lambda_k\cos\left(\frac{2\pi k}{N}+\varphi+\varphi_{\mathrm{m}}\right) + V\sum_{k=1}^{N}\lambda_k\cos\left(\frac{4\pi k}{N}+2\varphi+2\varphi_{\mathrm{m}}\right)\right]. \tag{15}$$

Different from Eqs. (10) and (13), no constant offset is presented in Eq. (15). As revealed by Eq. (15), the moiré artifact ΔV consists of two terms both dependent on the moiré phase φ_{m}. Both of the two terms contain a weighted mean of flux fluctuation factors. The first term is proportional to the quantity $\left(2-V^2\right)$, and introduces artifacts with a spatial frequency equal to that of the moiré phase φ_{m}. By contrast, the second term is proportional to the visibility V and introduces artifacts with a spatial frequency twice that of the moiré phase φ_{m}. As a comparison, the moiré artifact induced by phase-stepping errors is similar to Eq. (15) in terms of the spatial frequency. However, the artifact amplitudes resulting from phase-stepping error are substantially different from Eq. (15). While the first term with the same spatial frequency as the moiré phase is proportional to the squared visibility V^2, the second term with a doubled spatial frequency is proportional to the visibility V.

Furthermore, we estimate the moiré artifact of the retrieved dark-field image ΔD. According to Eq. (6), the dark-field signal D is retrieved from two independent phase-stepping measurements. Generally, the flux fluctuations occur in both object and reference measurements. The flux fluctuation factors within these two phase-stepping procedures are typically not correlated and therefore must be treated separately. As a consequence, the artifact in the retrieved dark-field image is a superposition of two independent artifacts, both being characterized by a weighted mean of flux fluctuation factors. Assuming that the errors in the object visibility V^{o} and the reference visibility V^{r} are small, the moiré artifact ΔD in the retrieved dark-field image can be estimated again by using the first-order Taylor approximation with respect to V^{o} and V^{r}. The resulting moiré artifact ΔD is given by

$$\Delta D = \frac{\Delta V^{\mathrm{o}}}{V^{\mathrm{r}}} - \frac{V^{\mathrm{o}}}{V^{\mathrm{r}}}\frac{\Delta V^{\mathrm{r}}}{V^{\mathrm{r}}} = D\left(\frac{\Delta V^{\mathrm{o}}}{V^{\mathrm{o}}} - \frac{\Delta V^{\mathrm{r}}}{V^{\mathrm{r}}}\right), \tag{16}$$

where

$$\frac{\Delta V^{\mathrm{o}}}{V^{\mathrm{o}}} = \frac{1}{N}\left[\left(\frac{2}{V^{\mathrm{o}}}-V^{\mathrm{o}}\right)\sum_{k=1}^{N}\lambda_k^{\mathrm{o}}\cos\left(\frac{2\pi k}{N}+\varphi+\varphi_{\mathrm{m}}\right) + \sum_{k=1}^{N}\lambda_k^{\mathrm{o}}\cos\left(\frac{4\pi k}{N}+2\varphi+2\varphi_{\mathrm{m}}\right)\right], \tag{17}$$

$$\frac{\Delta V^{\mathrm{r}}}{V^{\mathrm{r}}} = \frac{1}{N}\left[\left(\frac{2}{V^{\mathrm{r}}}-V^{\mathrm{r}}\right)\sum_{k=1}^{N}\lambda_k^{\mathrm{r}}\cos\left(\frac{2\pi k}{N}+\varphi_{\mathrm{m}}\right) + \sum_{k=1}^{N}\lambda_k^{\mathrm{r}}\cos\left(\frac{4\pi k}{N}+2\varphi_{\mathrm{m}}\right)\right]. \tag{18}$$

In practical applications, flux fluctuations can be induced by various external influences, and hence the flux fluctuation factors can be considered as stochastic. Moreover, the weighting factors are distinct for object and reference measurements. Therefore, moiré artifacts of object and reference visibility images do not mutually annihilate generally. As a result, the retrieved dark-field image always bears moiré artifacts in the case of flux fluctuations. Finally, as demonstrated by Eqs. (16)–(18), besides the dependence on the dark-field signal, the moiré artifact ΔD can even be influenced by object's refractive features which are not displayed in the dark-field modality and thus can appear independent of the expected morphology.

Finally, for the sake of completeness, we mention that flux fluctuations also introduce moiré artifacts into the retrieved transmission image T. Following a similar procedure and using Eq. (6), we can approximately estimate the moiré artifact of the transmission image ΔT resulting from flux fluctuations as

$$\Delta T = \frac{T}{N}\left[\sum_{k=1}^{N}\lambda_k^{\mathrm{o}}+V^{\mathrm{o}}\sum_{k=1}^{N}\lambda_k^{\mathrm{o}}\cos\left(\frac{2\pi k}{N}+\varphi+\varphi_{\mathrm{m}}\right)\right] - \frac{T}{N}\left[\sum_{k=1}^{N}\lambda_k^{\mathrm{r}}+V^{\mathrm{r}}\sum_{k=1}^{N}\lambda_k^{\mathrm{r}}\cos\left(\frac{2\pi k}{N}+\varphi_{\mathrm{m}}\right)\right], \tag{19}$$

where amplitude and shape are influenced by object's refractive and scattering features which are not displayed in the transmission modality.

3. Experimental results and discussion

To verify theoretical results and visualize the effect of flux fluctuations on the retrieved images, experiments were carried out at beamline BL13W1 of Shanghai Synchrotron Radiation Facility.[16] The x-ray grating interferometer consisted of a $\pi/2$-shifting phase grating with a period of 2.39 μm, and an analyzer grating with a period of 2.4 μm. The little difference in the grating periods was to match the beam divergence. The photon energy was 20 keV, and the distance between the two gratings was 46.4 mm. For data acquisition, a phase-stepping procedure was performed by translating the analyzer grating over one period. The phase step number is seven. Images were acquired with a scientific complementary metal–oxide–semiconductor (sCOMS) detector (Hamamatsu ORCA-Flash 4.0V2) with an effective pixel size of 13 μm. The exposure time was 3 ms for each image. The measured visibility had a mean value of 0.487 and a standard deviation of 0.032 over the

field-of-view. To investigate the spatial frequency of the moiré artifacts, the moiré phase φ_{m} was designed to be a parallel fringe pattern due to a pitch mismatch. As shown in Fig. 1, there were 20 moiré fringes within the field-of-view.

Within such a short exposure time, both the x-ray beam and the detector were sufficiently stable and precise. Therefore, we assumed no flux fluctuations in acquired phase-stepping data. Then the mean intensity, amplitude, phase and visibility images were retrieved using discrete Fourier transform based algorithm. These retrieved images did not bear moiré artifacts, and were used as ground truth images to calculate the theoretical moiré artifacts according to Eqs. (10), (13), (15), and (16), respectively.

To simulate flux fluctuations, the values of flux fluctuation factors were randomly chosen from the interval $[-0.1, 0.1]$ and listed in Table 1. According to Eq. (7), the phase-stepping data with flux fluctuations was simulated, and then used to retrieve the images containing moiré artifacts. The pixelwise difference of those images with moiré artifacts and their corresponding ground truth images were calculated to produce experimental moiré artifacts. Besides those values listed in Table 1, several other sets of flux fluctuation factors were also used to compare the theoretical and experimental moiré artifacts. They all presented equivalent results. Therefore, the set of flux fluctuation factors listed in Table 1 was exemplarily chosen to evaluate and discuss the results of this work.

Table 1. Flux fluctuation factors used for moiré artifacts estimations.

	λ_1	λ_2	λ_3	λ_4	λ_5	λ_6	λ_7
Reference	0	0.0390	−0.0366	0.0900	−0.0931	−0.0123	−0.0237
Object	0	0.0531	0.0590	−0.0626	−0.0020	−0.0109	0.0293

Figure 1 presents moiré artifacts of the retrieved mean intensity image in a reference measurement. Figure 1(a) shows the theoretical moiré artifact calculated by Eq. (10) and the ground truth images, and Fig. 1(b) shows the experimental moiré artifact. Visually speaking, the agreement of Figs. 1(a) and 1(b) is qualitatively good. For a quantitative evaluation, Fig. 2(a) shows the profile comparison along the dashed line marked in Fig. 1(a). The agreement of the two line profiles is quantitatively excellent, supported by the fact that the calculated correlation coefficient has a value of 0.9976. The existence of some locally minor discrepancies between theoretically calculated and experimental profiles can be explained by the first-order truncation of the Taylor series expansion used in the derivation of Eq. (10). Furthermore, Fig. 2(b) shows a plot of the Fourier spectra of the experimental profile. As expected by Eq. (10), the spectrum of the moiré artifact consists of two spatial frequencies. One is located at zero, and the other is equal to that of the moiré phase. By contrast, the moiré artifact induced by phase-stepping errors has a single spatial frequency equaling to that of the moiré phase.[31,32] These results validate the analytical model of the moiré artifact $\Delta\bar{I}$.

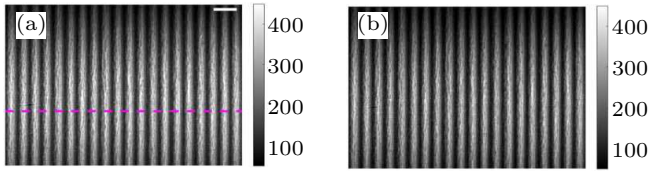


Fig. 1. Moiré artifacts of the retrieved mean intensity image. (a) Theoretical moiré artifact. (b) Experimental moiré artifact. Scale bar is 650 μm in panel (a).

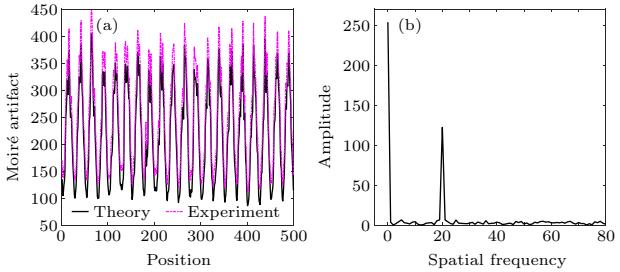


Fig. 2. (a) Line profile comparison between theoretical and experimental moiré artifacts. (b) Fourier spectra of the experimental profile.

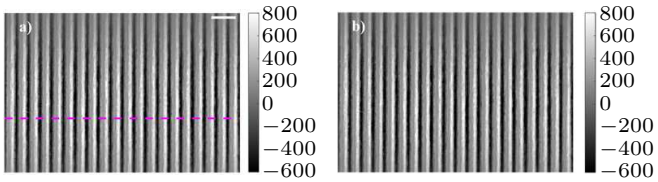


Fig. 3. Moiré artifact of the retrieved amplitude image. (a) Theoretical moiré artifact. (b) Experimental moiré artifact. Scale bar is 650 μm in panel (a).

Figure 3 displays moiré artifacts of the retrieved amplitude image in a reference measurement. Figure 3(a) shows the theoretical moiré artifact calculated by Eq. (13) and the ground truth images, and Fig. 3(b) shows the experimental moiré artifact. Qualitatively, the visual appearance of Figs. 3(a) and 3(b) agrees quite well. For a quantitative comparison, Fig. 4(a) depicts the profiles along the dashed line indicated in Fig. 3(a). The correlation coefficient of the line profiles is calculated to be 0.9974. The excellent agreement between the two profiles validates the theoretical formula of the moiré artifact ΔA. However, it is observed that there are some locally minor discrepancies between theoretical and experimental profiles. It is mainly attributed to the approximation of the first-order Taylor expansion used to derive Eq. (13). Moreover, Fig. 4(b) plots the experimental profile of the Fourier spectra. As expected from Eq. (13), the moiré artifact ΔA is a superposition of patterns of three distinct spatial frequencies. One is a global offset with a zero frequency, one has the same spatial frequency as that of the moiré phase, and the other has a spatial frequency twice that of the moiré phase. By comparison, the moiré artifact induced by phase-stepping errors consists of a single pattern with its spatial frequency twice that of the moiré phase.[31,32]

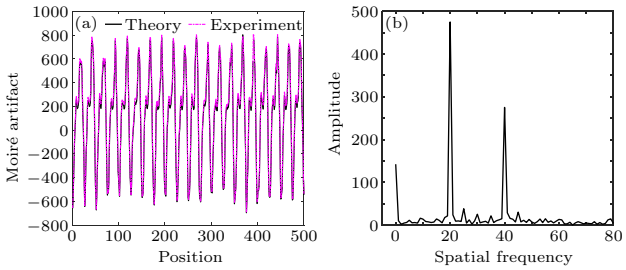


Fig. 4. (a) Line profile comparison between theoretical and experimental moiré artifacts. (b) Fourier spectra of the experimental profile.

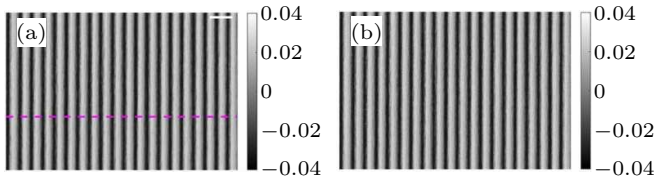


Fig. 5. Moiré artifact of the retrieved visibility image. (a) Theoretical moiré artifact (b) Experimental moiré artifact. Scale bar is 650 μm in panel (a).

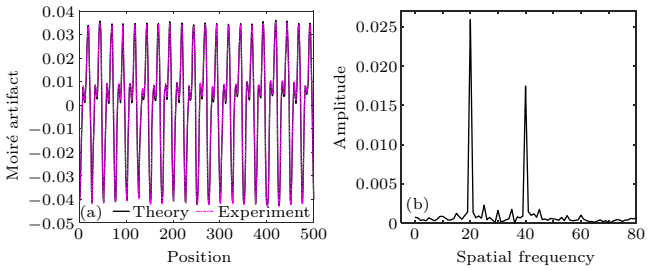


Fig. 6. (a) Line profile comparison between theoretical and experimental moiré artifacts. (b) Fourier spectra of the experimental profile.

The moiré artifacts of the retrieved visibility image are illustrated in Fig. 5. While Fig. 5(a) displays the theoretical moiré artifact calculated by using Eq. (15) and the ground truth images, Fig. 5(b) displays the experimental moiré artifact. As can be seen, the qualitative consistence between Figs. 5(a) and 5(b) is quite good. Furthermore, Fig. 6(a) shows a profile comparison along the dashed line marked in Fig. 5(a). The calculated correlation coefficient between the line profiles has a value of 0.9971. Thus, the quantitative agreement between theoretical and experimental profiles validates the theoretical model of the moiré artifact ΔV, despite some locally minor discrepancies. The Fourier spectra of the experimental profile is plotted in Fig. 6(b). As predicted by Eq. (15), there are two spatial frequencies in the spectrum of the moiré artifact ΔV. One is equal to that of the moiré phase, and the other is twice that of the moiré phase. And the amplitude of the doubled spatial frequency is lower than that of the same spatial frequency as the moiré phase.

Figure 7 displays the retrieved dark-field images and the moiré artifacts. Figure 7(a) shows the retrieved dark-field image with moiré artifact, and Fig. 7(b) shows the retrieved dark-field image without moiré artifact for a comparison. The pixel difference of Figs. 7(a) and 7(b) is calculated, and thus experimental moiré artifact resulting from flux fluctuations is obtained, and presented in Fig. 7(c). Figure 7(d) shows the theoretical moiré artifact calculated by using Eq. (16) and the ground truth images. A qualitative comparison between Figs. 7(c) and 7(d) demonstrates that theoretical moiré artefact agrees quite well with the experimental result.

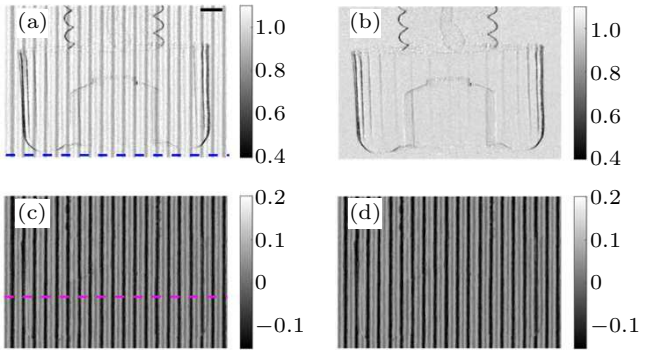


Fig. 7. (a) Dark-field image with moiré artifact. (b) Dark-field image without moiré artifact. (c) Experimental moiré artifact. (d) Theoretical moiré artifact. Scale bar is 650 μm in panel (a).

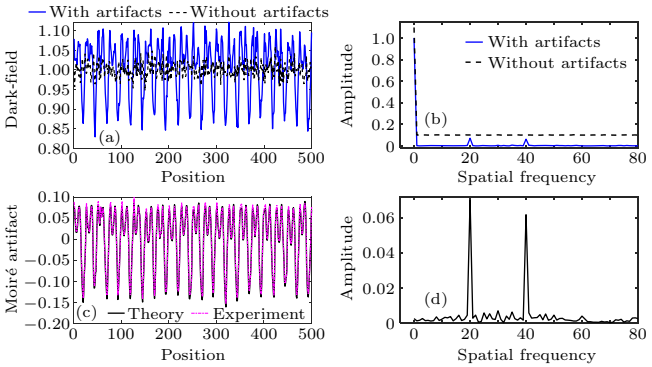


Fig. 8. (a) Line profile comparison between dark-field images with and without moiré artifacts. (b) Fourier spectra of the profiles shown in panel (a). (c) Line profile comparison between theoretical and experimental moiré artifacts. (d) Fourier spectra of the experimental profile in panel (c).

In order to gain some quantitative insight, Fig. 8(a) presents a profile comparison along the dashed line indicated in Fig. 7(a). Compared to the profile without artifacts, the profile with artifacts exhibits significantly increased variations resulting from flux fluctuations. Figure 8(b) plots the Fourier spectra of the profiles shown in Fig. 8(a). Note that the spectra of the profile without artifacts is offset vertically for ease of illustration. As expected, the spectrum without artifact has a single peak at the zero frequency. By contrast, there are two additional peaks resulting from flux fluctuations in the spectrum with artifacts. Moreover, for a quantitative assessment, Fig. 8(c) displays a profile comparison between theoretical and experimental moiré artifacts along the dashed line marked in Fig. 7(c). Despite a few slight local deviations, the theoretical profile is in good agreement with the experimental result. The correlation coefficient between the two profiles is calculated to be 0.9968. Therefore, the quantitative agreement confirms the validity of the theoretical model of the moiré artifact ΔD.

Besides, Fig. 8(d) plots the Fourier spectra of the experimental profile. As described by Eq. (16), the moiré artifact ΔD is a superposition of patterns of two spatial frequencies. One is equal to that of the moiré phase, and the other is twice that of the moiré phase.

4. Conclusion

We have presented comprehensive investigations of moiré artifacts induced by flux fluctuations in x-ray dark-field imaging using a grating interferometer. For the retrieved mean intensity, amplitude, visibility and dark-field images, analytical formulas of moiré artifacts are respectively derived by using the first-order Taylor series expansion. The validity of theoretical formulas is verified by results of synchrotron radiation experiments. Those results reveal that the moiré artifact of each image can be estimated by a weighted mean of flux fluctuation factors. And the weighting factors are dependent on the moiré phase that determines the basic shape of the moiré artifact. However, the amplitudes of weighting factors are significantly different for distinct retrieved images.

Furthermore, moiré artifacts can also be influenced by features that are not displayed in the particular contrast. As shown by Eq. (10), the moiré artifact of the mean intensity image is influenced by the visibility signal. For the amplitude image, Eq. (13) reveals that the moiré artifact induced by flux fluctuations is affected by the mean intensity and the amplitude signals simultaneously. By contrast, the moiré artifact induced by phase-stepping errors scales with the amplitude signal, and is independent of the mean intensity. In addition, as revealed by Eq. (16), the moiré artifact of the retrieved dark-field image is affected by object's refractive features as an argument of cosine functions. For the retrieved transmission image, Eq. (19) shows that the moiré artifact is affected by the object's refractive and scattering features simultaneously. Therefore, the visual appearance of moiré artifacts can be independent of the expected morphology. Those results emphasize the significance of the present investigations to facilitate a correct image interpretation.

Moreover, it demonstrates that the spatial frequency of the moiré artifacts differs for each retrieved image. The moiré artifacts of the amplitude, visibility and dark-field images contain a term with a spatial frequency twice that of the moiré phase. In particular, the moiré artifact of the amplitude image implies a term with its spatial frequency equal to that of the moiré phase. By contrast, this spatial frequency is absent in the spectrum of the moiré artifact induced by phase-stepping errors. Consequently, together with the increased strength, this knowledge can be used to identify the source of moiré artifacts.

Finally, since the flux fluctuation factors can not be often measured, future work will dedicate to the development of algorithms for the detection and removal of moiré artifacts. In combination with previous results,[33] the derived dependency of moiré artifacts on flux fluctuation factors can be used as guidelines for an accurate and efficient approximations of the moiré artifacts.

Acknowledgments

Project supported by the Natural Science Foundation of China (Grant Nos. U1532113, 11475170, and 11905041), Fundamental Research Funds for the Central Universities (Grant No. PA2020GDKC0024), and Anhui Provincial Natural Science Foundation (Grant No. 2208085MA18).

References

[1] Weitkamp T, Diaz A, David C, Pfeiffer F, Stampanoni M, Cloetens P and Ziegler E 2005 *Opt. Express* **13** 6296
[2] Pfeiffer F, Weitkamp T, Bunk O and David C 2006 *Nat. Phys.* **2** 258
[3] Pfeiffer F, Bech M, Bunk O, Kraft P, Eikenberry E F, Brönnimann Ch, Grünzweig C and David C 2008 *Nat. Mater.* **7** 134
[4] Donath T, Chabior M, Pfeiffer F, Bunk O, Reznikova E, Mohr J, Hempel E, Popescu S, Hoheisel M, Schuster M, Baumann J and David C 2009 *J. Appl. Phys.* **106** 054703
[5] Momose A, Yashiro W, Kuwabara H and Kawabata K 2009 *Jpn. J. Appl. Phys.* **48** 076512
[6] Yashiro W, Terui Y, Kawabata K and Momose A 2010 *Opt. Express* **18** 16890
[7] Ge X, Wang Z L, Gao K, Zhang K, Hong Y L, Wang D J, Zhu P P and Wu Z Y 2011 *Anal. Bioanal. Chem.* **401** 865
[8] Wang Z L, Gao K, Chen J, Ge X, Zhu P P, Tian Y C and Wu Z Y 2012 *Chin. Phys. B* **21** 118703
[9] Wang Z L, Gao K, Ge X, Wu Z, Chen H, Wang S H, Zhu P P, Yuan Q X, Huang W X, Zhang K and Wu Z Y 2013 *J. Phys. D: Appl. Phys.* **46** 494003
[10] Morimoto N, Fujino S, Ohshima K, Harada J, Hosoi T, Watanabe H and Shimura T 2014 *Opt. Lett.* **39** 4297
[11] Liu X, Guo J C, Lei Y H, Li J and Niu H B 2016 *Chin. Phys. B* **25** 028704
[12] Yang J, Guo J C, Lei Y H, Yi M H and Chen L 2017 *Chin. Phys. B* **26** 028701
[13] Wei C X, Wu Z, Fazi W, Wei W B, Bao Y, Luo R H, Wang L, Liu G and Tian Y C 2017 *Chin. Phys. B* **26** 108701
[14] Rong F, Gao Y, Guo C J, Xu W and Xu W 2019 *Chin. Phys. B* **28** 108702
[15] Faiz W, Li J, Gao K, Wu Z, Lei Y H, Huang J H and Zhu P P 2020 *Chin. Phys. B* **29** 014301
[16] Xi Y, Kou B Q, Sun H H, Qi J C, Sun J Q, Mohr J, Börner M, Zhao J, Xu L X, Xiao T Q and Wang Y J 2012 *J. Synchrotron Rad.* **19** 821
[17] Wang Z L, Zhou R C, Zhao L M, Ren K, Xu W, Liu B and Chen H 2021 *Chin. Phys. B* **30** 028702
[18] Yang J, Huang J H, Lei Y H, Zheng J B, Shan Y Z, Guo D Y and Guo J C 2022 *Chin. Phys. B* **31** 058701
[19] Arboleda C, Wang Z, Jefimovs K, Koehler T, Stevendaal U V, Kuhn N, David B, Prevrhal S, Lång K, Forte S, Kubik-Huch R A, Leo C, Singer G, Marcon M, Boss A, Roessl E and Stampanoni M 2020 *Eur. Radiol.* **30** 1419
[20] Rauch T, Rieger J, Pelzer G, Horn F, Erber R, Wunderle M, Emons J, Nabieva N, Fuhrich N, Michel T, Hartmann A, Fasching P and Antion G 2020 *Med. Phys.* **47** 1813
[21] Notohamiprodjo S, Webber N, Birnbacher L, Willner M, Viermetz M, Herzen J, Marschner M, Mayr D, Bartsch H, Saam T, Auweter S, Pfeiffer F, Reiser M and Hetterich H 2018 *Invest. Radiol.* **53** 26
[22] Yang F, Prade F, Griffa M, Jerjen I, Bella C Di, Herzen J, Sarapata A, Pfeiffer F and Lura P 2014 *Appl. Phys. Lett.* **105** 154105

[23] Ruiz-Yaniz M, Zanette I, Sarapata A, Birnbacher L, Marschner M, Chabior M, Olbinado M, Pfeiffer F and Rack A 2016 *J. Synchrotron Rad.* **23** 1202
[24] Bachche S, Nonoguchi M, Kato K, Kageyama M, Koike T, Kuribayashi M and Momose A 2017 *Sci. Rep.* **7** 6711
[25] Miller E A, White T A, McDonald B S and Seifert A 2013 *IEEE Trans. Nucl. Sci.* **60** 416
[26] Hellbach K, Beller E, Schindler A, Schoeppe F, Hesse N, Baumann A, Schinner R, Auweter S, Hauke C, Radicke M and Meinel F 2018 *Invest. Radiol.* **53** 352
[27] Gradl R, Morgan K S, Dierolf M, Jud C, Hehn L, Günther B, Möller W, Kutschke D, Yang L, Stoeger T, Pfeiffer D, Gleich B, Achterhold K, Schmid O and Pfeiffer F 2019 *IEEE Trans. Med. Imaging* **38** 649
[28] Willer K, Fingerle A, Noichl W, *et al.* 2021 *Lancet Digit. Health* **3** e733
[29] Frank M, Urban T, Willer K, *et al.* 2021 *Med. Phys.* **48** 6152
[30] Weber T, Bartl P, Bayer F, Durst J, Haas W, Michel T, Ritter A and Anton G 2011 *Med. Phys.* **38** 4133
[31] Hauke C, Leghissa M, Pelzer G, Radicke M, Weber T, Mertelmeier T, Anton G and Ritschl L 2017 *Opt. Express* **25** 32897
[32] Marco F, Marschnr M, Birnbacher L, Noël P, Herzen J and Pfeiffer F 2018 *Opt. Express* **26** 12707
[33] Hashimoto K, Takano H and Momose A 2020 *Opt. Express* **28** 16363
[34] Viermetz M, Gustschin N, Schmid C, Haeusele J, Teuffenbach M, Meyer P, Bergner F, Lasser T, Proksa R, Koehler T and Pfeiffer F 2022 *Proc. Natl. Acad. Sci. USA* **119** e2118799119